

OPEN ACCESS

**Repository of the Max Delbrück Center for Molecular Medicine (MDC)
in the Helmholtz Association**

<http://edoc.mdc-berlin.de/15684>

Electrodynamics and radiofrequency antenna concepts for human magnetic resonance at 23.5 T (1 GHz) and beyond

Winter, L. and Niendorf, T.

This is the final version of the accepted manuscript. The original article has been published in final edited form in:

Magnetic Resonance Materials in Physics, Biology and Medicine
2016 JUN ; 29(3): 641-656
2016 APR 20 (first published online)
Publisher: [Springer Verlag](#)

The final publication is available at Springer via: <https://doi.org/10.1007/s10334-016-0559-y>

Copyright © 2016 [ESMRMB](#)

Electrodynamics and Radiofrequency Antenna Concepts for Human Magnetic Resonance at 23.5 Tesla (1 GHz) and Beyond

Lukas Winter¹ and Thoralf Niendorf^{1,2,3}

¹ Berlin Ultrahigh Field Facility (B.U.F.F.), Max-Delbrück Center for Molecular Medicine, Berlin, Germany

² Experimental and Clinical Research Center (ECRC), a joint cooperation between the Charité and the Max Delbrück Center for Molecular Medicine, Berlin, Germany

³ MRI.TOOLS GmbH, Berlin, Germany

Corresponding Author:

Prof. Dr. Thoralf Niendorf

Berlin Ultrahigh Field Facility (B.U.F.F.)

Max-Delbrück Center for Molecular Medicine

Robert-Roessle-Strasse 10

13125 Berlin

Germany

Tel.: +49 30 9406 4505

E-mail: Thoralf.Niendorf@mdc-berlin.de

Word count abstract: 199

Word count text: 4836

Number of figures: 11

Number of tables: 2

Running Title: Towards magnetic resonance at 23.5 Tesla

Key words: electrodynamics, magnetic resonance, electron paramagnetic resonance ultrahigh field MR, radiofrequency antenna

Abstract

Object

This work investigates electrodynamic constraints, explores RF antenna concepts and examines transmission fields (B_{1+}) and RF power deposition of dipole antenna arrays for ^1H magnetic resonance of the human brain at 1GHz (23.5T).

Materials and Methods

Electromagnetic field simulations (EMF) are performed in phantoms with average tissue simulants for dipole antennae using discrete frequencies (300MHz (7.0T) to 3GHz (70.0T)). To advance to a human setup EMF simulations are conducted in anatomical human voxel models of the human head using a 20-element dipole array operating at 1 GHz.

Results

Our results demonstrate that transmission fields suitable for ^1H MR of the human brain can be achieved at 1GHz. An increase in transmit channel density around the human head helps to enhance B_{1+} in the center of the brain. The calculated relative increase in specific absorption rate (SAR) at 23.5T vs. 7.0T was below 1.4 (in-phase phase setting) and 2.7 (circular polarized phase setting) for the dipole antennae array.

Conclusion

The benefits of multi-channel dipole antennae at higher frequencies render MR at 23.5T feasible from an electrodynamic standpoint. This very preliminary finding opens the door on further explorations that might be catalyzed into a 20 Tesla class human MR system.

Introduction

While everyday clinical MR is generally carried out at 1.5 T, 3.0 T and 7.0 T machines have become mainstays of experimental and clinical research. More than 35,000 7.0 Tesla MR research examinations (1) have already been performed globally, producing valuable data that indicate the value of ultrahigh fields (2-8). Even if these instruments do not become standard tools in the everyday clinical setting in the very near future, the invaluable new insights they are providing into (patho)physiological processes will be helpful to patients everywhere. This trend will continue as UHF-MR extends beyond 7.0 T.

The move to higher magnetic field strengths will directly depend on our ability to solve a number of technical and theoretical problems. Some of the benefits are already clear: we have already seen progress in remotely probing local concentrations of fluorine, sodium, potassium and chlorine in human tissues (9-14), in assessing bioenergetic conditions (15-17) and oxygen consumption (18) *in vivo* along with the advances in 9.4 T human MR (15,19-24). Pioneering reports on MR physics, radio-frequency (RF) power deposition considerations and novel RF antenna designs (25,26) spurred the installation of a 10.5 T whole-body MR system at the Center for Magnetic Resonance Research, University of Minnesota, Minneapolis, USA (27). An 11.7 T brain MRI initiative is being spearheaded by the French Alternative Energies and Atomic Energy Commission (CEA, NeuroSpin, Gif/Yvette, France) and by the National Institutes of Health (NIH, Bethesda, USA). Recent numerical and experimental explorations up to 14.0 T showed the potential of UHF-MR for imaging and targeting human tissue through focal radiofrequency (RF) induced heat deposition and very local manipulations of temperature (28). Magnetic field strengths as high as 20 Tesla were demonstrated to be conceptually appealing for offsetting the inherent spatial resolution constraints of positron emission tomography (29,30). Physical considerations and numerical simulations up to 23.5 T (1 GHz) manifest the potential of targeted RF heating for localized RF

hyperthermia of intracranial lesions as an adjunct cancer therapy and provided convincing reasons for thermal magnetic resonance (thermalMR) to study the role of temperature in biological systems and disease (31).

Joint efforts of the nuclear magnetic resonance and biomedical magnetic resonance imaging communities identified the science drivers, technological challenges and prospects for achieving MRI at 20 Tesla (32,33).

Although it is particularly timely to consider moving to a 20 Tesla class MR system the benefits and sensitivity gain of UHF-MR at $B_0 > 11.7$ T are faced with a multitude of challenges. These include the need for innovations in magnet technology involving high-temperature superconductors. We must also gain a better understanding of electrodynamic constraints that arise through an increase in spin excitation frequency. There will be power losses as the conductive properties of tissues change in a frequency-dependent manner, and we will need to resolve a number of legitimate issues concerning RF power deposition restrictions, transmission field (B_{1+}) efficiency constraints, depth penetration limitations and radiation losses. Due to wavelength shortening at frequencies in the 0.5 to 1 GHz range (e.g. ca. 5cm at 1 GHz) the imaging location transitions from the near field to the far field region of the RF antenna.

These challenges are motivating research into electrodynamics at ultrahigh fields and are catalysing innovations in RF antenna design, which must be specially tailored for very high frequencies. Here we elucidate the electrodynamic constraints for frequencies ranging from 300 MHz (7.0 T) up to 3 GHz (70.0 T) and explores the benefits of multi-element dipole antenna arrays at short RF wave lengths. To meet this goal electromagnetic field (EMF) simulations are conducted in phantoms and in human voxel models to detail transmission field and specific absorption rate (SAR) distributions of multi-element antenna arrays.

Materials and Methods

Theory

Increasing the frequency in MRI beyond today's limits has a number of implications on electromagnetic field transmission and absorption as schematically outlined in Figure 1. These implications sometimes drive the notion that human UHF-MR at $B_0 > 11.7$ T might be a limit *per se*. This judgement is premature in advance of a careful theoretical and practical study of electrodynamics at ultrahigh fields. Typical MR applications and RF coil designs at clinical field strengths ($B_0 = 1.5$ T or $B_0 = 3.0$ T) deal with the near field regime at frequencies of 64 MHz and 128 MHz, respectively. At 300 MHz and higher frequencies the transition between the near and far field regime changes design considerations for RF coils, making it necessary to take into account wave propagation effects. At high frequencies the wavelength of the electromagnetic field in tissue generated by a transmit (TX) element starts to become similar or short compared to the size of the target anatomy (Figure 1). This leads to interferences which induce B_{1+} non-uniformities. To address this obstacle multi-element transceiver coil arrays have been developed. These developments took advantage of building blocks that include stripline elements (34-38), dielectric resonant antennae (39), loop elements (40-46) and electrical dipoles (47-53).

Electrical dipole antennae were reported to provide a valuable alternative to traditional loop coils or stripline elements (47). Dipole antennae exhibit a simple RF antenna design with good directivity where the Poynting vector is perpendicular to the dipole length. This trait is in particular useful at higher frequencies, where relevant imaging regions are outside the near field (e.g. ≈ 46 mm at 1 GHz) of the antenna (Figure 2). Wave propagation patterns need to be considered when applying the advantages of multi-element arrays for B_{1+} focussing. The energy transmission of loop coils is not directed towards a single target (Figure 2a), which is also reflected in the B_{1+} pattern (Figure 2b). Here there is an advantage of dipoles or antennae with improved directivity

towards the imaging target, since a multi-antennae configuration permits a dedicated use of constructive interferences (Figure 2c&d) – in other words, making use of the interference to focus E- or H-field components of independent transmission elements to a single target. The E-field distribution along the main axis of a dipole can be approximated by a harmonic linear polarized plane wave propagating perpendicular to the long axis of the dipole (Figure 2c). With the simplification of the propagation along the z-direction and the polarization direction along the dipole length (y-direction) the Helmholtz equation becomes (54):

$$\frac{\partial^2 E_y}{\partial z^2} - \gamma^2 E_y = 0 \quad (1)$$

with the complex E-field E_z . The solution is then:

$$E_y(z) = A_1 e^{-\gamma z} + A_2 e^{\gamma z} \quad (2)$$

with the propagation constant γ :

$$\gamma^2 = (\alpha + j\beta)^2 = -\omega^2 \epsilon \mu + j\omega \mu \sigma \quad (3)$$

The angular frequency ω , the permittivity $\epsilon = \epsilon_0 \epsilon_r$, the permeability $\mu = \mu_0 \mu_r$ and the electrical conductivity σ determine the attenuation constant α and the phase constant β :

$$\alpha = \omega \sqrt{\frac{\mu \epsilon}{2} \left[\sqrt{1 + \left(\frac{\sigma}{\omega \epsilon}\right)^2} - 1 \right]} \quad (4)$$

$$\beta = \omega \sqrt{\frac{\mu \epsilon}{2} \left[\sqrt{1 + \left(\frac{\sigma}{\omega \epsilon}\right)^2} + 1 \right]} \quad (5)$$

Equations 4 and 5 can be taken as a basis to derive the electrodynamic effects associated with an increase in MR transmission frequency (Figure 1). The wavelength λ

$$\lambda = \frac{2\pi}{\beta} \quad (6)$$

of a lossy medium depends on the frequency, permittivity and electric conductivity (Equation 5). The relative permittivity has a strong influence on wavelength shortening by $\sim 1/\sqrt{\epsilon_r}$ ($f = \text{const}$) in the lossless case ($\sigma = 0$) when transitioning from air ($\epsilon_r \approx 1$) to tissue

($\epsilon_r \approx 44$, white matter). This leads to pronounced B_1^+ field inhomogeneities across imaging volumes larger than the wavelength such as the human head or the human body if single element RF transmitters are used. When moving to higher magnetic fields ($f \neq \text{const}$) the wavelength in tissue (e.g. at 3 GHz vs. 300 MHz in white matter) decreases further. This is a combined effect of decreasing relative permittivity (~25% from 300 MHz to 3 GHz for brain white matter (55)), increasing electrical conductivity (~370% from 300 MHz to 3 GHz for brain white matter (55)) and increasing frequency with the latter being the dominant effect for further wavelength shortening (Equation 5 & Equation 6) (Figure 1).

The aforementioned relative increase in conductivity leads to higher power losses P_{loss} (Figure 1) resulting in higher SAR:

$$SAR = \frac{P_{loss}}{\rho} = \frac{\sigma |\vec{E}|^2}{\rho} \quad (7)$$

with the tissue density ρ and $|\vec{E}|^2$ the amplitude of the electric field vector. At the same time these power losses lead to reduced $B_1^+/\sqrt{P_{in}}$ amplitudes (Equation 4, Figure 1). This behaviour increases SAR if the same target flip angle is to be reached (Figure 1) while on the receive (RX) side reduced B_1^- decreases some of the SNR gains intrinsic to higher magnetic fields. These drawbacks can be offset to some extent by increasing the number of transmitter and receiver elements in multi-element RF antenna arrays.

The merits of dipole antenna arrays are not limited to the transmission side. On the receiver side, ultimate intrinsic signal-to-noise ratio (UISNR) considerations reveal that current patterns are dominated by the linear (dipole type) curl-free current patterns for $B_0 \geq 9.4$ T (56,57), while at 7.0 T loop- and dipole current patterns contribute equally to UISNR (56,57). This observation opens an avenue to a more efficient use of electric dipole like receiver elements in UHF-MR (56).

All these reasons render electrical dipole antennae legitimate candidates for implementation in transceiver arrays tailored for MR at ultrahigh and extreme magnetic field strengths that may help to relax challenges associated with RF power deposition constraints. The reduction in RF wavelength reduces the area of superficial SAR, which

together with increased power losses leads to decreased coupling between antennae (Figure 1). This permits an increase in the number of transmitter/receiver elements positioned around an object (Figure 3) while element coupling is not enhanced. This improvement in coil density can be leveraged for enhancing B_{1+} homogeneity (58), SNR (59,60), parallel imaging capabilities (52,61,62), parallel transmit performance (58) and transmission efficiency ($B_{1+}/\sqrt{P_{in}}$) at the imaging location where a constructive interference of all single waves can be accomplished. In addition, the dipole antenna length is reduced at higher RF frequencies (Figure 3), which decreases the field of view along the long axis of the antenna but also boosts $B_{1+}/\sqrt{P_{in}}$ for regions underneath the dipole due to higher current densities per input power. The reduced field of view can be compensated for by placing extra rings of antenna elements along the z-direction.

Electromagnetic Field Simulations in Virtual Phantoms

Electromagnetic field (EMF) simulations were performed using the finite integration technique of CST Microwave Studio 2012 (CST GmbH, Darmstadt, Germany) (63). For this purpose $\lambda/2$ dipole antennae were modelled in a cylindrical shape (diameter=4mm) as a perfect electrical conductor (PEC) and positioned at 1cm distance to a uniform cylindrical phantom (diameter = 180 mm, length = 600 mm) (Figure 3). Permittivity ($\epsilon_{phantom}$) and conductivity ($\sigma_{phantom}$) of the phantom were frequency adjusted according to (64):

$$\epsilon_{phantom}(f) = 0.6 \cdot \epsilon_{white\ matter}(f) + 0.4 \cdot \epsilon_{grey\ matter}(f) \quad (8)$$

$$\sigma_{phantom}(f) = 0.6 \cdot \sigma_{white\ matter}(f) + 0.4 \cdot \sigma_{grey\ matter}(f) \quad (9)$$

B_{1+} and SAR distributions were evaluated for (i) a single dipole (Figure 3a), (ii) a symmetrical 8-element dipole array (Figure 3b) and (iii) a symmetrical max-element dipole antenna array (Figure 3c). For the max-element setup the number of transmit elements was governed by the condition that decoupling remains below $S_{xy} = -13dB$. The simulated RF frequencies were $f=300,400,500,600,700,800,900,1000,1200,1400,1600,1800,2000$ and 3000 MHz with the max-element setup being simulated at $f = 300$ MHz, 1000 MHz, 2000 MHz and 3000 MHz. The port impedance was set to 73 Ω . All

antennae were matched and tuned to $S_{11} < -30\text{dB}$. Dipole antenna length was adjusted to the given frequency as illustrated in Figure 3d-f and surveyed in Table I. All antenna array configurations were driven in circular polarized (CP) mode and in-phase (00) with 0° phase shift between transmit elements. The inclusion of the bore (inner diameter = 684mm) induces only a minor increase in $B_{1^+}/\sqrt{P_{in}}$ amplitude (+4% (00) and 0% (CP) at 300MHz vs. +6% (00) and 7% (CP) at 1GHz). With this finding the bore diameter was not modelled to save computational time. Local SAR (1 g average) was calculated for 1 W accepted input power at the port with a phantom density of $\rho = 1041 \text{ kg/m}^3$. Relative SAR increase was defined by:

$$\text{rel. SAR increase} = \frac{\max SAR_{1g}(f_2)}{\max SAR_{1g}(f_1 = 300\text{MHz})} \cdot \left(\frac{\max B_{1,center}^+(f_1 = 300\text{MHz})}{\max B_{1,center}^+(f_2)} \right)^2 \quad (10)$$

Maximum $B_{1^+}/\sqrt{P_{in}}$ and maximum SAR_{1g} obtained for the phantom were evaluated by using a circular region of interest (diameter = 90 mm) positioned in the center of the phantom as indicated in Figure 4e.

Electromagnetic Field Simulations in Human Voxel Models

To advance from phantom setups to a human setup EMF simulations were carried out using the finite integration of CST Microwave Studio 2012 (CST GmbH, Darmstadt, Germany) in two *in vivo* human voxel models ("Ella" and "Duke") from the virtual family (65). For this purpose a 20-element dipole antenna array (inner radius = 128 mm) operating at 1 GHz was positioned around the head of the human voxel model using the frequency adjusted tissue parameters shown in Table II (65,66). For comparison an 8-element bow tie electric dipole antenna array was positioned around Ella's and Duke's head using the same radius and a frequency of 300 MHz. The length of the 1 GHz dipole antenna building block ($l = 142 \text{ mm}$) was approximated to the total length of the bow tie dipoles ($l = 156 \text{ mm}$). Both configurations were driven in-phase (0° phase shift between transmit elements) and in a circularly polarized (CP) mode (phase shift

between transmit channels: $360^\circ/\text{number of elements}$). No RF shimming was performed. For both configurations $B_1^+/\sqrt{P_{in}}$ and local SAR ($P_{in} = 1\text{W}$) averaged over 1g brain tissue (SAR1g) were calculated. The CST legacy SAR averaging algorithm (67) was employed to avoid artificially high SAR values near air interfaces (68). The algorithm increases the averaging cube at the boundary until a biological mass of 1g is reached. For RF power deposition assessment, averaging over 1g was chosen to detail and better capture SAR hotspots at higher RF frequencies, which would have been otherwise suppressed for 10g averaging volumes. A cylindrical phantom (diameter = 240 mm, length = 400mm) was positioned around the head of the human voxel model to keep the simulation setup as close as possible to the phantom simulation study. The phantom material (300 MHz: $\epsilon = 50.3$, $\sigma = 0.1\text{ S/m}$, 1 GHz: $\epsilon = 44.1$, $\sigma = 0.1\text{ S/m}$) ensures comparable wave propagation and high coupling efficiency into the head of the human voxel model.

Results

Electromagnetic Field Simulations in Virtual Phantoms

Higher RF frequencies reduce the dipole size significantly (Figure 3 d-f, Table I). While the dipole length is 41 cm at 300 MHz it is shortened to 14.2 cm at 1 GHz and to 4.4 cm at 3 GHz. This behaviour affords larger densities for antenna arrays at higher RF frequencies. The results of the simulation study are displayed in Figure 4 and Figure 5. The transmission field $B_{I^+}/\sqrt{P_{in}}$ decreases with frequency for the single element and 8-element setup (Figure 5a-b). For the 8-element setup at 300 MHz maximum $B_{I^+}/\sqrt{P_{in}}$ (CP) in the center of the phantom was found to be $18.3 \mu\text{T}/\sqrt{\text{kW}}$ (Figure 5a). For the same region maximum $B_{I^+}/\sqrt{P_{in}}$ was reduced to $16.9 \mu\text{T}/\sqrt{\text{kW}}$ at 1000 MHz, $6.9 \mu\text{T}/\sqrt{\text{kW}}$ at 2000 MHz and $1.3 \mu\text{T}/\sqrt{\text{kW}}$ at 3000 MHz (Figure 5a). Maximum SAR1g increased by more than 400% for a single element when moving from 300 MHz ($\text{SAR1g}_{max} = 3.2\text{W/kg}$) to 1 GHz ($\text{SAR1g}_{max} = 13\text{W/kg}$). At 3 GHz peak SAR1g was 55.7W/kg for the single element configuration (Figure 5c-d). With the 8-element configuration peak SAR1g (CP) was reduced for the same input power to 0.22W/kg (300 MHz), 1.53W/kg (1 GHz) and 7.1W/kg (3 GHz). For the same configuration the $B_{I^+}/\sqrt{\text{SAR1g}_{max}}$ ratio (CP) decreased from $1.23 \mu\text{T}/\sqrt{(\text{W/kg})}$ (300 MHz) to $0.43 \mu\text{T}/\sqrt{(\text{W/kg})}$ (1 GHz) as shown in Figure 5e. A $B_{I^+}/\sqrt{\text{SAR1g}_{max}}$ ratio of $0.11 \mu\text{T}/\sqrt{(\text{W/kg})}$ and $0.02 \mu\text{T}/\sqrt{(\text{W/kg})}$ was observed at 2 GHz and at 3 GHz (Figure 5e).

The max-element configuration improved $B_{I^+}/\sqrt{P_{in}}$ and lowered SAR1g_{max} significantly. Placing 19 dipole elements ($f = 1 \text{GHz}$) equidistantly around the phantom yielded a $B_{I^+}/\sqrt{P_{in}}$ of $19.3 \mu\text{T}/\sqrt{\text{kW}}$ (CP) in the center region of the phantom (Figure 4i and Figure 5a), which is superior to $B_{I^+}/\sqrt{P_{in}}$ provided by the 8-element configuration at 300 MHz (Figure 4f and Figure 5a). SAR1g_{max} was 0.7W/kg for the 19-element setup (CP) at 1 GHz, which corresponds to $\sim 45\%$ SAR1g_{max} of the 8-element configuration at 1 GHz. In total the 19-element setup improved $B_{I^+}/\sqrt{\text{SAR1g}_{max}}$ (CP) to $0.73 \mu\text{T}/\sqrt{(\text{W/kg})}$ at 1 GHz as shown in Figure 5e.

A closer examination of the ratio between central SAR and surface SAR (Figure 5f) revealed that central SAR was higher than surface SAR for frequencies up to 700 MHz when using the 8-element setup. Increasing the number of elements to 19 provided a center-to-surface SAR ratio of ~ 1.4 at 1 GHz. This improvement versus the 8-element configuration shows that energy can be transmitted efficiently to the center of the phantom by the max-element setup using superposition principles. These results also indicate that the application of thermal interventions (thermalMR) induced by controlled RF power deposition can be potentially performed at 1 GHz and above (28,31).

The relative SAR increase induced by moving to $f > 300$ MHz is displayed in Figure 5g-h. For the 8-element antenna setup the relative SAR increase at 1 GHz was found to be 3.8 (00) and 8.2 (CP) versus 300 MHz. Increasing the number of dipole elements to 19 resulted in a relative SAR increase of only 1.8 (00) and 2.8 (CP) at 1 GHz versus 300 MHz.

At 2 GHz and 3 GHz the maximum number of elements was 22, which presents a minor increase in element density versus 1 GHz (Table I). A saturation of the number of channels occurs for these frequencies, which is governed by meeting the condition of similar decoupling between elements at lower frequencies. Since the antenna distance to the object was not changed with increasing frequency, loading effects are less pronounced and have smaller influence on decoupling values. In an unloaded case (only air surrounding the antennae) and without any adjustments of the tuning/matching network, S_{11} increases from < -30 dB (loaded) to -1.8 dB (unloaded) at 300 MHz. At 1 GHz unloaded $S_{11} = -12.9$ dB, showing still fairly good transmission properties with minor reflections. At 3 GHz unloaded $S_{11} = -13.2$ dB, which is only a slight improvement towards 1 GHz.

In order to address the reduced imaging volume coverage of the single ring shorter dipole antennae at 1GHz, the number of dipole elements along the z-direction can be potentially increased (Figure 6). Under similar decoupling restrictions (decoupling ≤ -13 dB) 57 elements were distributed around the phantom as depicted in

Figure 6. For this purpose three rings each accommodating 19 elements tuned to 1GHz were applied (Figure 6). This configuration exhibits the same spatial dimensions (inner diameter, outer diameter, RF antenna array length) as the 300 MHz 8-element array configuration. Driving all 57 elements simultaneously and each ring in CP-mode reduces $B_{I^+}/\sqrt{P_{in}}$ by a factor $\sim\sqrt{3}$ and SAR ($P_{in} = 1W$) by a factor of 3 versus transmission through the central ring only (Figure 6). This leads to overall similar relative SAR increase for both driving conditions (Figure 6).

Electromagnetic Field Simulations in Human Voxel Models

The results of the human voxel model simulations are summarized in Figure 7-10. Both antenna array configurations exhibit similar length (Figure 7a,b). The number of transmit elements can be increased from 8-elements at 300 MHz to 20-elements at 1 GHz with a decoupling of $S_{xy} < -14dB$. B_{I^+} field distributions for Ella and Duke (in-phase) are shown in Figure 7c and Figure 8c for 300 MHz and Figure 7d and Figure 8d for 1 GHz respectively. As a characteristic of the in-phase phase setting an E-field hotspot is generated in the center of the brain due to constructive interferences of the wave propagation. This leads to an H -field void and hence B_{I^+} void at the center with circular H -field components around it showing a characteristic B_{I^+} ring around the center with the ring size depending on the RF wavelength. Around the cancellation region a $B_{I^+}/\sqrt{P_{in}}$ of $13.1 \mu T/\sqrt{kW}$ (Ella) and $12.5 \mu T/\sqrt{kW}$ (Duke) was obtained for 300 MHz. For the same region a $B_{I^+}/\sqrt{P_{in}}$ of $12.3 \mu T/\sqrt{kW}$ (Ella) and $12.1 \mu T/\sqrt{kW}$ (Duke) was observed at 1 GHz. For the circular polarized mode (Figure 9 and Figure 10), constructive interference of B_{I^+} occurred in the center of the head (Figure 9c and Figure 10c) along with the characteristic E-field or SAR ring pattern (Figure 9h and Figure 10h). At 300 MHz maximum $B_{I^+}/\sqrt{P_{in}}$ in the center was $18.5 \mu T/\sqrt{kW}$ (Ella) and $20.1 \mu T/\sqrt{kW}$ (Duke). At 1 GHz a $B_{I^+}/\sqrt{P_{in}}$ of $17.5 \mu T/\sqrt{kW}$ (Ella) and $17.6 \mu T/\sqrt{kW}$ (Duke) was observed. These findings demonstrate that even at higher RF frequencies, high $B_{I^+}/\sqrt{P_{in}}$ is feasible in the center of the brain. 3D SAR1g distributions are depicted in Figure 7e-f (Ella) and Figure 8e-f (Duke)

for in-phase and Figure 9e-f (Ella) and Figure 10e-f (Duke) for CP-mode. At 300 MHz maximum SAR_{1g} of 0.78 W/kg (Ella) and 0.71 W/kg (Duke) was found in the center of the brain for the in-phase mode (Figure 7g and Figure 8g). For the CP mode at 300 MHz maximum SAR_{1g} of 0.49 W/kg (Ella) and 0.44 W/kg (Duke) was found in regions close to the surface of the head (Figure 9g and Figure 10g). At 1 GHz central SAR_{1g} was 0.76 W/kg (Ella) and 0.92 W/kg (Duke). Regions at the surface of the head showed a SAR_{1g} of 0.88 W/kg (Ella) and 0.89 W/kg (Duke) for the in-phase mode and 0.96 W/kg (Ella) and 0.90 W/kg (Duke) for the CP mode (Figure 7-10g-h). The 20-element array enabled a more uniform surface SAR distribution due to the many element setup, which reduces SAR_{1g} compared to an 8-element setup at 1GHz. Overall, the relative SAR increase for 1 GHz vs. 300 MHz for the in-phase mode was 1.3 (Ella) and 1.4 (Duke). In the CP mode the relative SAR increase was 2.2 (Ella) and 2.7 (Duke). Notwithstanding the B_{1+} voids and lower B_{1+} homogeneity at 1 GHz (e.g. Figure 7d), RF power can be efficiently focused to the center of the brain by the 20-element setup which results in high $B_{1+}/\sqrt{P_{in}}$ by means of constructive interference of the waves propagated. This behaviour relaxes the SAR penalties and allows $B_{1+}/\sqrt{SAR_{1g_{max}}}$ properties similar to the 8-element configuration employed at 7.0 T. Loading conditions using the bow tie antennae at 300MHz did not change significantly ($S_{11} < -19.6$ dB) when Ella was replaced with Duke (without alteration of the tuning/matching network).

RF Power Loss Considerations

Our investigations on transmit efficiency $B_{1+}/\sqrt{P_{in}}$ are referring to the accepted power at the antenna port. Eventually transmit efficiency will be defined by the RF power output of the RF power amplifier. In addition to the investigated power losses in tissue that mitigate transmit efficiency with increasing frequency, power losses increase in cables, RF antennae and RF components (e.g. capacitors) due to a reduced skin depth and an increase in dissipation factor (69). On top of these power losses it is expected that radiation losses will increase with increasing frequency (70,71). The

radiation power losses using the bow tie electric dipole antennae loaded with the voxel model Ella in full bore simulations were 8% (00) and 13% (CP) at 300 MHz and increased to 31% (00) and 29% (CP) for the max-element configuration at 1GHz (Figure 11).

Discussion

Our analysis of the electrodynamics relative to human tissue properties and RF antennae configurations appropriate for very high MRI magnetic fields focused on frequencies ranging from 300 MHz (7.0 T) to 3 GHz (70.0 T). Our numerical electromagnetic field simulations add to the literature by detailing transmission field and specific absorption rate distributions of dipole and bow tie antenna arrays placed around phantoms and *in vivo* human voxel models. Our findings show that the combination of lower $B_1^+/\sqrt{P_{in}}$ and increased local SAR at higher frequencies necessitate a higher RF power deposition to achieve the same flip angle at higher fields. Our simulations indicate that transmission fields suitable for ^1H MRI of the human brain can be achieved at 1 GHz (23.5 T) from the theoretical point of view. Improved decoupling between elements at higher frequencies facilitates an enhanced transmit channel density around the human head. This approach affords more equally distributed RF power over the surface of the target while constructive summation of each propagated wave increases $B_1^+/\sqrt{P_{in}}$ in the center of the human head.

Another finding of our study is that if benchmarked against the 300 MHz baseline, the increase in RF power deposition per generated B_1^+ field is less than the traditionally cited $SAR \sim B_0^2$ relationship (72). At 1 GHz a relative SAR increase of 3.8 (00) and 8.2 (CP) versus 300 MHz was obtained in the phantom for an 8-element antenna configuration. Enlarging the number of dipole elements placed around the same phantom resulted in a relative SAR increase of only 1.8 (00) and 2.8 (CP) at 1 GHz versus 300 MHz. In short, our results show that the SAR increase obtained for frequencies up to $f = 1$ GHz is even below a $SAR \sim B_0$ relationship for dedicated RF antenna array designs. While keeping decoupling below -13dB the number of dipole antennae equally distributed in the x-y plane could be increased from eight elements at 300 MHz to nineteen elements at 1 GHz. In a similar way dipole shortening at higher RF frequencies can be put to good use to place more elements along the z-direction. This approach supports the

distribution of 57 elements (3 rings each accommodating 19 elements tuned to 1 GHz) instead of 8-elements at 300 MHz (decoupling $\leq -13\text{dB}$) while both array configurations exhibit similar volume coverage (same inner/outer radius and same total length of the antenna array).

Our human voxel model studies confirmed that SAR penalties at higher frequencies can be offset by using a high density array of dipole antennae. This setup facilitated $B_1^+/\sqrt{\text{SAR}}I_{g_{max}}$ properties similar to an 8-element configuration employed at 7.0 T. The simulations revealed an increase in relative SAR of < 2 (00) and < 3 (CP) at 1 GHz vs. 300 MHz. Our findings are in accordance with previous numerical simulations or experimental results obtained at 4 T, 7 T, 8 T and 11.7 T (58,73-75). For example EMF simulations in head models reported that the slope of absorbed RF power decreases with increasing frequency covering a range from 64 MHz (1.5 T) to 345 MHz (8.0 T) (75). Ultimate intrinsic SAR considerations showed SAR flattening or slight reduction with increasing frequencies ranging from 42 MHz (1.0 T) to 500 MHz (11.7 T) (58).

Our voxel model simulations make use of a dielectric surrounding the imaging volume to allow for a fair comparison with the phantom simulation study. While the dielectric approach used in this study can be conveniently implemented for imaging of the extremities and other target regions outside of the head, minor adjustments to the geometry and shape of the dielectric need to be made for human head imaging to assure patient comfort. Of course, the proposed RF antenna array can be also operated without a dielectric which might influence $B_1^+/\sqrt{\text{SAR}}$. Another practical implication of eliminating the dielectric is an increase in RF antenna sensitivity to loading effects, which can be reduced by e.g. geometrically adjustable antennas (35,76).

It is a recognized limitation that transmission field uniformity was not included within the scope of this study. Obviously, a broad spectrum of methodology has been established to mitigate transmission field non-uniformity including but not limited to static/dynamic B_1^+ shimming approaches (77-79), RF excitation using time interleaved

acquisition of modes (80), multi-spoke parallel transmission (81) or RF pulse design (82). This methodology is compatible with the RF coil configurations proposed in this study.

The implications of our research into the electrodynamic constraints of high RF frequencies are not limited to MR. They are relevant to electron paramagnetic resonance (EPR) imaging which is considered to be a potential contributor to the understanding of the in vivo biochemistry particularly in the study of free radicals (83). On the clinical side tissue redox states could be examined in areas not explored heretofore (e.g. concussion, heart failure, cancer).

The progress in this work provides encouragement for the MR physics, (biomedical) engineering and imaging communities on the road to a human 23.5 T MR system. Admittedly, a 23.5 T class human MR system is, for the moment, merely a vision. It is nonetheless a vision that should inspire basic research in several directions, including numerical simulations, as a way of preparing the ground for predictable future advances in MR technology. The problems raised so far have already motivated new research for improvements in RF coil concepts, and advances in superconductors. Apart from the technology developments, active research is required for understanding the physiological effects of very high magnetic fields including the need for detailing the field dependencies of magneto-hydrodynamic effects and forces on tissues with differing magnetic susceptibilities at $B_0 > 14.0$ T.

Conclusion

While novel magnet technology will surely continue to develop in the future, its uses might well be constrained by technical challenges and practical obstacles. Here we show that MRI of the human brain is feasible from an electrodynamic and theoretical standpoint utilizing frequencies larger than 500 MHz, providing that multi-channel dipole antennae are arranged accordingly. This should render investigations with MRI at 23.5 T and EPR at 1 GHz possible. This very preliminary finding opens the door on further explorations that might be catalyzed into a 20 Tesla class human MR system.

Acknowledgement

This work was funded (in part, T.N.) by the Helmholtz Alliance ICEMED – Imaging and Curing Environmental Metabolic Diseases, through the Initiative and Network Fund of the Helmholtz Association (ICEMED-Project 1210251). The authors wish to thank Russell Hodge (Max-Delbrück Center for Molecular Medicine in the Helmholtz Association, Berlin, Germany) for brainstorming as well as for editing and proof reading the manuscript.

Conflict of Interest

Thoralf Niendorf is founder and CEO of MRI.TOOLS GmbH, Berlin, Germany.

References

1. Schaaf M, Siemens Healthcare GmbH, Imaging and Therapy Systems, Magnetic Resonance, Erlangen, Germany, personal communication, August, 2015.
2. Moser E, Stahlberg F, Ladd ME, Trattnig S. 7-T MR--from research to clinical applications? *NMR Biomed* 2012;25(5):695-716.
3. Niendorf T, Graessl A, Thalhammer C, Dieringer MA, Kraus O, Santoro D, Fuchs K, Hezel F, Waiczies S, Ittermann B, Winter L. Progress and promises of human cardiac magnetic resonance at ultrahigh fields: a physics perspective. *J Magn Reson* 2013;229:208-222.
4. Kraff O, Fischer A, Nagel AM, Monninghoff C, Ladd ME. MRI at 7 tesla and above: Demonstrated and potential capabilities. *J Magn Reson Imaging* 2015;41(1):13-33.
5. Sinnecker T, Kuchling J, Dusek P, Dorr J, Niendorf T, Paul F, Wuerfel J. Ultrahigh field MRI in clinical neuroimmunology: a potential contribution to improved diagnostics and personalised disease management. *The EPMA journal* 2015;6(1):16.
6. Kremer S, Renard F, Achard S, Lana-Peixoto MA, Palace J, Asgari N, Klawiter EC, Tenenbaum SN, Banwell B, Greenberg BM, Bennett JL, Levy M, Villoslada P, Saiz A, Fujihara K, Chan KH, Schippling S, Paul F, Kim HJ, de Seze J, Wuerfel JT, Cabre P, Marignier R, Tedder T, van Pelt D, Broadley S, Chitnis T, Wingerchuk D, Pandit L, Leite MI, Apiwattanakul M, Kleiter I, Prayoonwiwat N, Han M, Hellwig K, van Herle K, John G, Hooper DC, Nakashima I, Sato D, Yeaman MR, Waubant E, Zamvil S, Stuve O, Aktas O, Smith TJ, Jacob A, O'Connor K. Use of Advanced Magnetic Resonance Imaging Techniques in Neuromyelitis Optica Spectrum Disorder. *JAMA neurology* 2015;72(7):815-822.
7. Trattnig S, Bogner W, Gruber S, Szomolanyi P, Juras V, Robinson S, Zbyn S, Haneder S. Clinical applications at ultrahigh field (7 T). Where does it make the difference? *NMR Biomed* 2015.
8. Niendorf T, Paul K, Oezerdem C, Graessl A, Klix S, Huelnhagen T, Hezel F, Rieger J, Waiczies H, Frahm J, Nagel A, Oberacker E, Winter L. W(h)ither Human Cardiac and Body Magnetic Resonance at Ultrahigh Fields? Technical Advances, Practical Considerations, Applications, and Clinical Opportunities *NMR Biomed* 2015, DOI: 10.1002/nbm.3268 [epub ahead of print].
9. Kopp C, Linz P, Wachsmuth L, Dahlmann A, Horbach T, Schofl C, Renz W, Santoro D, Niendorf T, Muller DN, Neining M, Cavallaro A, Eckardt KU, Schmieder RE, Luft FC, Uder M, Titze J. ²³Na magnetic resonance imaging of tissue sodium. *Hypertension* 2012;59(1):167-172.
10. Umathum R, Rosler MB, Nagel AM. In vivo ³⁹K MR imaging of human muscle and brain. *Radiology* 2013;269(2):569-576.
11. Nagel AM, Lehmann-Horn F, Weber MA, Jurkat-Rott K, Wolf MB, Radbruch A, Umathum R, Semmler W. In Vivo CI MR Imaging in Humans: A Feasibility Study. *Radiology* 2014:131725.
12. Ji Y, Waiczies H, Winter L, Neumanova P, Hofmann D, Rieger J, Mekte R, Waiczies S, Niendorf T. Eight-channel transceiver RF coil array tailored for ¹H/¹⁹F MR of the human knee and fluorinated drugs at 7.0 T. *NMR in biomedicine* 2015;28(6):726-737.
13. Graessl A, Ruehle A, Waiczies H, Resetar A, Hoffmann SH, Rieger J, Wetterling F, Winter L, Nagel AM, Niendorf T. Sodium MRI of the human heart at 7.0 T: preliminary results. *NMR in biomedicine* 2015;28(8):967-975.

14. Linz P, Santoro D, Renz W, Rieger J, Rühle A, Ruff J, Deimling M, Rakova N, Müller DN, Luft FC, Titze J, Niendorf T. Skin sodium measured with ^{23}Na MRI at 7.0 T. *NMR Biomed* 2015;28(1):54-62.
15. Lu A, Atkinson IC, Zhou XJ, Thulborn KR. PCr/ATP ratio mapping of the human head by simultaneously imaging of multiple spectral peaks with interleaved excitations and flexible twisted projection imaging readout trajectories at 9.4 T. *Magn Reson Med* 2013;69(2):538-544.
16. Rodgers CT, Clarke WT, Snyder C, Vaughan JT, Neubauer S, Robson MD. Human cardiac ^{31}P magnetic resonance spectroscopy at 7 Tesla. *Magn Reson Med* 2014;72(2):304-315.
17. Schmid AI, Meyerspeer M, Robinson SD, Goluch S, Wolzt M, Fiedler GB, Bogner W, Laistler E, Krssak M, Moser E, Trattnig S, Valkovic L. Dynamic PCr and pH imaging of human calf muscles during exercise and recovery using P gradient-Echo MRI at 7 Tesla. *Magn Reson Med* 2015.
18. Atkinson IC, Thulborn KR. Feasibility of mapping the tissue mass corrected bioscale of cerebral metabolic rate of oxygen consumption using $^{17}\text{-oxygen}$ and $^{23}\text{-sodium}$ MR imaging in a human brain at 9.4 T. *Neuroimage* 2010;51(2):723-733.
19. Atkinson IC, Sonstegaard R, Pliskin NH, Thulborn KR. Vital signs and cognitive function are not affected by $^{23}\text{-sodium}$ and $^{17}\text{-oxygen}$ magnetic resonance imaging of the human brain at 9.4 T. *J Magn Reson Imaging* 2010;32(1):82-87.
20. Atkinson IC, Claiborne TC, Thulborn KR. Feasibility of $^{39}\text{-potassium}$ MR imaging of a human brain at 9.4 Tesla. *Magn Reson Med* 2014;71(5):1819-1825.
21. Scheffler K, Ehses P. High-resolution mapping of neuronal activation with balanced SSFP at 9.4 tesla. *Magn Reson Med* 2015.
22. Pohmann R, Speck O, Scheffler K. Signal-to-noise ratio and MR tissue parameters in human brain imaging at 3, 7, and 9.4 tesla using current receive coil arrays. *Magn Reson Med* 2015.
23. Shah NJ. Multimodal neuroimaging in humans at 9.4 T: a technological breakthrough towards an advanced metabolic imaging scanner. *Brain structure & function* 2015;220(4):1867-1884.
24. Thulborn K, Lui E, Guntin J, Jamil S, Sun Z, Claiborne TC, Atkinson IC. Quantitative sodium MRI of the human brain at 9.4 T provides assessment of tissue sodium concentration and cell volume fraction during normal aging. *NMR Biomed* 2015.
25. Tian J, Shrivastava D, Strupp J, Zhang J, Vaughan JT. From 7T to 10.5T: B1+, SAR and Temperature Distribution for Head and Body MRI. In Proceedings of the 20th Annual Meeting of ISMRM, Melbourne, Victoria, Australia 2012:2666.
26. Tian F, Lagore L, Vaughan JT. Dipole arrays for MR head imaging: 7.0 T vs. 10.5T. In Proceedings of the 23rd Annual Meeting of the ISMRM, Toronto, Canada 2015:3116.
27. Vaughan JT, Delabarre L, Tian F, Sohn SM, Shrivastava D, Adriany G, Ugurbil K. Toward 10.5 T MRI. In Proceedings of the 22nd Annual Meeting of the ISMRM, Milan, Italy 2014:4822.
28. Winter L, Özerdem C, Hoffmann W, Santoro D, Müller A, Waiczies H, Seemann R, Graessl A, Wust P, Niendorf T. Design and Evaluation of a Hybrid Radiofrequency Applicator for Magnetic Resonance Imaging and RF Induced Hyperthermia: Electromagnetic Field Simulations up to 14.0 Tesla and Proof-of-Concept at 7.0 Tesla. *PLOS ONE* 2013;8(4):e61661.
29. Rickey DW, Gordon R, Huda W. On the lifting the inherent limitations of Positron Emission Tomography by using magnetic fields (MagPET). *Automedica* 1992;14(1):355-369.

30. Shah NJ, Herzog H, Weirich C, Tellmann L, Kaffanke J, Caldeira L, Kops ER, Qaim SM, Coenen HH, Iida H. Effects of magnetic fields of up to 9.4 T on resolution and contrast of PET images as measured with an MR-BrainPET. *PLoS One* 2014;9(4):e95250.
31. Winter L, Oezerdem C, Hoffmann W, van de Lindt T, Periquito J, Ji Y, Ghadjar P, Budach V, Wust P, Niendorf T. Thermal magnetic resonance: physics considerations and electromagnetic field simulations up to 23.5 Tesla (1GHz). *Radiat Oncol* 2015;10(1):201.
32. Committee to Assess the Current Status and Future Direction of High Magnetic Field Science in the United States; Board on Physics and Astronomy; Division on Engineering and Physical Sciences; National Research Council. Washington, DC, USA: The National Academies Press 2013. 232 p.
33. Polenova T, Budinger TF. Ultrahigh field NMR and MRI: Science at a crossroads. Report on a jointly-funded NSF, NIH and DOE workshop, held on November 12-13, 2015 in Bethesda, Maryland, USA. *J Magn Reson* 2016.
34. Gregor Adriany P, Moortele F, Steen Moeller J, Peter Andersen C, Xiaoliang Zhang W, Klaas P, Peter Boesiger T. Transmit and receive transmission line arrays for 7 Tesla parallel imaging. *Magnetic Resonance in Medicine* 2005;53(2):434-445.
35. Gregor Adriany P, Moortele J, Steen Moeller E, Can Akgün C, Thomas Vaughan K. A geometrically adjustable 16-channel transmit/receive transmission line array for improved RF efficiency and parallel imaging performance at 7 Tesla. *Magn Reson Med* 2008;59(3):590-597.
36. Snyder CJ, DelaBarre L, Metzger GJ, van de Moortele PF, Akgun C, Ugurbil K, Vaughan JT. Initial results of cardiac imaging at 7 Tesla. *Magn Reson Med* 2009;61(3):517-524.
37. Vaughan JT, Snyder CJ, DelaBarre LJ, Bolan PJ, Tian J, Bolinger L, Adriany G, Andersen P, Strupp J, Ugurbil K. Whole-body imaging at 7T: preliminary results. *Magn Reson Med* 2009;61(1):244-248.
38. Wiggins GC, Potthast A, Triantafyllou C, Wiggins CJ, Wald LL. Eight-channel phased array coil and detunable TEM volume coil for 7 T brain imaging. *Magnetic Resonance in Medicine* 2005;54(1):235-240.
39. Aussenhofer SA, Webb AG. An eight-channel transmit/receive array of TE01 mode high permittivity ceramic resonators for human imaging at 7T. *J Magn Reson* 2014;243:122-129.
40. Versluis M, Tsekos N, Smith N, Webb A. Simple RF design for human functional and morphological cardiac imaging at 7 tesla. *Journal of Magnetic Resonance* 2009;200(1):161-166.
41. Winter L, Kellman P, Renz W, Grassl A, Hezel F, Thalhammer C, von Knobelsdorff-Brenkenhoff F, Tkachenko V, Schulz-Menger J, Niendorf T. Comparison of three multichannel transmit/receive radiofrequency coil configurations for anatomic and functional cardiac MRI at 7.0T: implications for clinical imaging. *Eur Radiol* 2012;22(10):2211-2220.
42. Thalhammer C, Renz W, Winter L, Hezel F, Rieger J, Pfeiffer H, Graessl A, Seifert F, Hoffmann W, von Knobelsdorff-Brenkenhoff F, Tkachenko V, Schulz-Menger J, Kellman P, Niendorf T. Two-dimensional sixteen channel transmit/receive coil array for cardiac MRI at 7.0 T: design, evaluation, and application. *Journal of magnetic resonance imaging : JMRI* 2012;36(4):847-857.
43. Grassl A, Winter L, Thalhammer C, Renz W, Kellman P, Martin C, von Knobelsdorff-Brenkenhoff F, Tkachenko V, Schulz-Menger J, Niendorf T. Design, evaluation and

- application of an eight channel transmit/receive coil array for cardiac MRI at 7.0 T. *Eur J Radiol* 2013;82(5):752-759.
44. Shajan G, Kozlov M, Hoffmann J, Turner R, Scheffler K, Pohmann R. A 16-channel dual-row transmit array in combination with a 31-element receive array for human brain imaging at 9.4 T. *Magnetic Resonance in Medicine* 2013.
 45. Brown R, Deniz CM, Zhang B, Chang G, Sodickson DK, Wiggins GC. Design and Application of Combined 8-Channel Transmit and 10-Channel Receive Arrays and Radiofrequency Shimming for 7-T Shoulder Magnetic Resonance Imaging. *Investigative radiology* 2014;49(1):35-47.
 46. Zhao W, Cohen-Adad J, Polimeni JR, Keil B, Guerin B, Setsompop K, Serano P, Mareyam A, Hoecht P, Wald LL. Nineteen-channel receive array and four-channel transmit array coil for cervical spinal cord imaging at 7T. *Magnetic Resonance in Medicine* 2013.
 47. Raaijmakers A, Ipek O, Klomp D, Possanzini C, Harvey P, Lagendijk J, van den Berg C. Design of a radiative surface coil array element at 7 T: The single side adapted dipole antenna. *Magn Reson Med* 2011;66(5):1488-1497.
 48. Özerdem C, Winter L, Hoffmann W, Waiczies H, Seeman R, Santoro D, Müller A, Ok A, Lindel T, Ittermann B, Niendorf T. Design and Evaluation of a Dipole Antenna TX/RX Element as a Building Block for Combined MR Imaging and RF Hyperthermia at 7.0 T. In *Proceedings of the 20th Annual Meeting of ISMRM, Melbourne, Victoria, Australia 2012*:2641.
 49. Ipek O, Raaijmakers AJ, Klomp DW, Lagendijk JJ, Lujten PR, van den Berg CA. Characterization of transceive surface element designs for 7 tesla magnetic resonance imaging of the prostate: radiative antenna and microstrip. *Phys Med Biol* 2012;57(2):343-355.
 50. Winter L, Özerdem C, Hoffmann W, Santoro D, Müller A, Waiczies H, Seemann R, Graessl A, Wust P, Niendorf T, Yacoub E. Design and Evaluation of a Hybrid Radiofrequency Applicator for Magnetic Resonance Imaging and RF Induced Hyperthermia: Electromagnetic Field Simulations up to 14.0 Tesla and Proof-of-Concept at 7.0 Tesla. *PLoS ONE* 2013;8(4):e61661.
 51. Ipek O, Raaijmakers AJ, Lagendijk JJ, Lujten PR, van den Berg CA. Intersubject local SAR variation for 7T prostate MR imaging with an eight-channel single-side adapted dipole antenna array. *Magn Reson Med* 2014;71(4):1559-1567.
 52. Özerdem C, Winter L, Graessl A, Paul K, Els A, Weinberger O, Rieger J, Kühne A, Dieringer M, Hezel F, Voit D, Frahm J, Niendorf T. 16 Channel Bow Tie Antenna Transceiver Array for Cardiac Magnetic Resonance at 7.0T. *Magn Reson Med* 2015:[Epub ahead of print].
 53. Raaijmakers AJ, Italiaander M, Voogt IJ, Lujten PR, Hoogduin JM, Klomp DW, van den Berg CA. The fractionated dipole antenna: A new antenna for body imaging at 7 Tesla. *Magn Reson Med* 2015:[Epub ahead of print].
 54. Sadiku MN. *Elements of electromagnetics*: Oxford university press New York; 2001.
 55. Gabriel S, Lau R, Gabriel C. The dielectric properties of biological tissues: II. Measurements in the frequency range 10 Hz to 20 GHz. *Physics in Medicine and Biology* 1996;41:2251.
 56. Lattanzi R, Sodickson DK. Ideal current patterns yielding optimal signal-to-noise ratio and specific absorption rate in magnetic resonance imaging: Computational methods and physical insights. *Magn Reson Med* 2012;68(1):286-304.

57. Graham Charles Wiggins BZ, Riccardo Lattanzi, Gang Chen, and Daniel Sodickson. The Electric Dipole Array: An Attempt to Match the Ideal Current Pattern for Central SNR at 7 Tesla. 2012. p 541.
58. Lattanzi R, Sodickson D, Grant A, Zhu Y. Electrodynamics constraints on homogeneity and radiofrequency power deposition in multiple coil excitations. *Magn Reson Med* 2009;61(2):315-334.
59. Roemer P, Edelstein W, Hayes C, Souza S, Mueller O. The NMR phased array. *Magn Reson Med* 1990;16(2):192-225.
60. Winter L, Kellman P, Renz W, Gräßl A, Hezel F, Thalhammer C, Von Knobelsdorff Brenkenhoff F, Tkachenko V, Schulz-Menger J, Niendorf T. Comparison of three multichannel transmit/receive radiofrequency coil configurations for anatomic and functional cardiac MRI at 7.0T: implications for clinical imaging. *Eur Radiol* 2012;22(10):2211-2220.
61. Zhu Y, Hardy CJ, Sodickson DK, Giaquinto RO, Dumoulin CL, Kenwood G, Niendorf T, Lejay H, McKenzie CA, Ohliger MA, Rofsky NM. Highly parallel volumetric imaging with a 32-element RF coil array. *Magnetic resonance in medicine : official journal of the Society of Magnetic Resonance in Medicine / Society of Magnetic Resonance in Medicine* 2004;52(4):869-877.
62. Sodickson DK, Hardy CJ, Zhu Y, Giaquinto RO, Gross P, Kenwood G, Niendorf T, Lejay H, McKenzie CA, Ohliger MA, Grant AK, Rofsky NM. Rapid volumetric MRI using parallel imaging with order-of-magnitude accelerations and a 32-element RF coil array: feasibility and implications. *Academic radiology* 2005;12(5):626-635.
63. Clemens M, Weiland T. Discrete electromagnetism with the finite integration technique. *Prog Electromagn Res* 2001;32:65-87.
64. Miller AKH, Alston RL, Corsellis JAN. Variation with age in the volumes of grey and white matter in the cerebral hemispheres of man: measurements with an image analyser. *Neuropath Appl Neuro* 1980;6(2):119-132.
65. Christ A, Kainz W, Hahn E, Honegger K, Zefferer M, Neufeld E, Rascher W, Janka R, Bautz W, Chen J. The Virtual Family—development of surface-based anatomical models of two adults and two children for dosimetric simulations. *Phys Med Biol* 2010;55:N23-38.
66. Hasgall P, Neufeld E, Gosselin MC, Klingenböck A, Kuster N. IT'IS Database for thermal and electromagnetic parameters of biological tissues. <http://www.itis.ethz.ch/database>. Version 2.4, Published July 30th, 2013. Accessed January 1, 2014
67. Wittig T. SAR Overview. CST User Manual 2007.
68. Oh S, Carluccio G, Collins CM. Method and Tool for Improved, Rapid N-gram Average SAR Determination. *Proc Intl Soc Mag Reson Med* 2011;#3868.
69. Eaton R, Kmiec C. *Electrical Losses in Coaxial Cables*. 2008; Providence, USA.
70. Liu W, Kao Cp, Collins CM, Smith MB, Yang QX. On consideration of radiated power in RF field simulations for MRI. *Magnetic Resonance in Medicine* 2013;69(1):290-294.
71. Kuehne A, Goluch S, Waxmann P, Seifert F, Ittermann B, Moser E, Laistler E. Power balance and loss mechanism analysis in RF transmit coil arrays. *Magnetic Resonance in Medicine* 2015;74(4):1165-1176.
72. Hoult D, Lauterbur PC. The sensitivity of the zeugmatographic experiment involving human samples. *Journal of Magnetic Resonance (1969)* 1979;34(2):425-433.
73. Hoult DI. Sensitivity and Power Deposition in a High-Field Imaging Experiment. *Journal of Magnetic Resonance Imaging* 2000;12(1):46-67.

74. Vaughan JT, Garwood M, Collins C, Liu W, DelaBarre L, Adriany G, Andersen P, Merkle H, Goebel R, Smith M. 7T vs. 4T: RF power, homogeneity, and signal-to-noise comparison in head images. *Magnetic Resonance in Medicine* 2001;46(1):24-30.
75. Collins CM, Smith MB. Signal-to-noise ratio and absorbed power as functions of main magnetic field strength, and definition of "90°" RF pulse for the head in the birdcage coil. *Magnetic Resonance in Medicine* 2001;45(4):684-691.
76. Adriany G, DelaBarre L, Eryaman Y, Lagore R, Erturk A, Metzger GJ, Vaughan JT, Ugurbil K, Van de Moortele PF. Initial Imaging Results with a 10.5T Geometrically Adjustable Dipole Array. *Proc ISMRM UHF Workshop* 2016.
77. van den Bergen B, van den Berg CA, Klomp DW, Lagendijk JJ. SAR and power implications of different RF shimming strategies in the pelvis for 7T MRI. *J Magn Reson Imaging* 2009;30(1):194-202.
78. Metzger GJ, Auerbach EJ, Akgun C, Simonson J, Bi X, Ugurbil K, van de Moortele PF. Dynamically applied B1+ shimming solutions for non-contrast enhanced renal angiography at 7.0 Tesla. *Magn Reson Med* 2013;69(1):114-126.
79. Graessl A, Renz W, Hezel F, Dieringer M, Winter L, Oezerdem C, Kellman P, Santoro D, Lindel T, Frauenrath T, Pfeiffer H, Niendorf T. Modular 32 Channel Transceiver Coil Array for Cardiac MRI at 7T. *Magn Reson Med* 2014;72(1):276-290.
80. Orzada S, Maderwald S, Poser BA, Bitz AK, Quick HH, Ladd ME. RF excitation using time interleaved acquisition of modes (TIAMO) to address B1 inhomogeneity in high-field MRI. *Magn Reson Med* 2010;64(2):327-333.
81. Wu X, Schmitter S, Auerbach EJ, Ugurbil K, Van de Moortele PF. Mitigating transmit B1 inhomogeneity in the liver at 7T using multi-spoke parallel transmit RF pulse design. *Quantitative imaging in medicine and surgery* 2014;4(1):4-10.
82. Setsompop K, Alagappan V, Gagoski B, Witzel T, Polimeni J, Potthast A, Hebrank F, Fontius U, Schmitt F, Wald LL, Adalsteinsson E. Slice-selective RF pulses for in vivo B1+ inhomogeneity mitigation at 7 tesla using parallel RF excitation with a 16-element coil. *Magn Reson Med* 2008;60(6):1422-1432.
83. Eaton SS, Eaton GR. The world as viewed by and with unpaired electrons. *Journal of Magnetic Resonance* 2012;223:151-163.

Figure Captions

Figure 1: Schematic of the influence of an increased RF frequency on physical and MR imaging parameters. Disadvantages like decreasing $B_{1^+}/\sqrt{P_{in}}$ amplitude and B_{1^+} homogeneity and increasing SAR can be offset by antenna array design using dipoles.

Figure 2: Comparison of E- (left) and B_{1^+} -field (right) transmission patterns of a loop (top) and a dipole (bottom) antenna at 1 GHz in a rectangular phantom ($\epsilon_r = 44.1$, $\sigma = 0.1$ S/m). To guide the eye near-field, transition and far-field zones are highlighted. The energy transmission of the loop element is not directed towards a single target (a), which is also reflected in the B_{1^+} pattern (b). The E-field pattern of the dipole can be approximated by a harmonic linear polarized plane wave propagating perpendicular to the long axis of the dipole (c). Unlike the loop element the B_{1^+} transmission pattern of the dipole shows good directivity with the Poynting vector being perpendicular to the main axis of the dipole.

Figure 3: top: Schematic of the simulation setup of a (a) single element, (b) 8-element and (c) max-element dipole antenna array (exemplary shown for $f = 1$ GHz) positioned symmetrically around a phantom (length = 600 mm). **bottom:** Comparison of the dipole length for (d) 300 MHz (length = 410 mm), (e) 1 GHz (length = 142 mm) and (f) 3 GHz (length = 44 mm).

Figure 4: Simulated **(a-l)** B_{1^+} and **(m-r)** SAR distributions of a 1-element, 8-element and max-element dipole antenna array. At higher RF frequencies the size of the dipole antennae is reduced (a-c). The dipole shortening affords an increased current distribution per input power and higher $B_{1^+}/\sqrt{P_{in}}$ per volume as demonstrated for an 8-element dipole array at **a)** 300 MHz, **b)** 1 GHz and **c)** 3 GHz. B_{1^+} distributions are shown for a central axial slice using 1-, 8- and max-element arrays (CP mode) at **d-f)** 300 MHz,

e-h) 1 GHz and **i-k)** 3 GHz. Comparison of the SAR ($P_{in}=1W$) distribution (in-phase mode) of **m,p)** 1-element, **n,q)** 8-element and **o,r)** max-element dipole antenna arrays at 1 GHz. While surface SAR can be reduced significantly using a higher number of transmit elements under the condition < -13 dB, constructive interferences of the wave propagation in the phantom demonstrates that SAR/P_{in} and $B_1^+/\sqrt{P_{in}}$ at the center can be increased. Maximum $B_1^+/\sqrt{P_{in}}$ and maximum SAR/P_{in} for CP and in-phase mode for all frequencies were evaluated inside a circular region of interest (diameter = 90 mm) positioned in the center of the phantom as indicated by the dashed circle in e).

Figure 5: EMF simulation results of the phantom study for discrete frequencies ranging from $f = 300$ to $f = 3000$ MHz. **a)** Maximum $B_1^+/\sqrt{P_{in}}$ in a central region of the phantom, **b)** ratio $B_1^+-center/B_1^+-surface$, **c-d)** maximum SAR/g for an input power of $P_{in} = 1$ W, **e)** $B_1^+/\sqrt{SAR/g_{max}}$, **f)** center vs. surface SAR ratio and **g-h)** relative SAR increase vs. 300 MHz.

Figure 6: Comparison of SAR ($P_{in} = 1W$) (**top**) and $B_1^+/\sqrt{P_{in}}$ (**bottom**) obtained for an 8-element dipole antenna array at 300 MHz (**left**) with a same sized (inner and outer diameter, RF antenna array length) 57-element dipole antenna array at 1 GHz (**middle, right**). (**left**) B_1^+ and SAR distribution (CP) of the 8-element array at 300 MHz, (**middle**) B_1^+ and SAR distribution (CP) of the 57-element array at 1 GHz transmitting through all elements and (**right**) B_1^+ and SAR distribution (CP) of the 57-element array at 1 GHz where transmission is constrained to the central ring consisting of 19 dipole antennae. Please note that decoupling for both antenna arrays is $S_{xy} \leq -13$ dB.

Figure 7: Comparison of an **a)** 8-element bow tie dipole and a **b)** 20-element dipole antenna array positioned around the voxel model "Ella". An in-phase (0° phase shift between transmit elements) phase setting was employed. **c-d)** B_1^+ distributions in an axial slice of maximum central B_1^+ . SAR/g distribution ($P_{in} = 1W$) at **e-f)** the surface of the voxel model and **g-h)** through the axial slice of maximum SAR/g . The circle in **g-h)**

illustrates the phantom material (Table II) positioned around Ella's head. Please note that the shoulders of Ella were included in the EMF simulations.

Figure 8: Comparison of an **a)** 8-element bow tie dipole and a **b)** 20-element dipole antenna array positioned around the voxel model "Duke". An in-phase (0° phase shift between transmit elements) phase setting was employed. **c-d)** B_1^+ distributions in an axial slice of maximum central B_1^+ . SAR1g distribution ($P_{in} = 1W$) at **e-f)** the surface of the voxel model and **g-h)** through the axial slice of maximum SAR1g. The circle in **g-h)** illustrates the phantom material (Table II) positioned around Duke's head. Please note that the shoulders of Duke were included in the EMF simulations.

Figure 9: Comparison of an **a)** 8-element bow tie dipole and a **b)** 20-element dipole antenna array positioned around the voxel model "Ella". A circular polarized phase setting (phase shift between transmit channels: $360^\circ/\text{number of elements}$) was employed. **c-d)** B_1^+ distributions in an axial slice of maximum central B_1^+ . SAR1g distribution ($P_{in} = 1W$) at **e-f)** the surface of the voxel model and **g-h)** through the axial slice of maximum SAR1g. The circle in **g-h)** illustrates the phantom material (Table II) positioned around Ella's head. Please note that the shoulders of Ella were included in the EMF simulations.

Figure 10: Comparison of an **a)** 8-element bow tie dipole and a **b)** 20-element dipole antenna array positioned around the voxel model "Duke". A circular polarized (phase shift between transmit channels: $360^\circ/\text{number of elements}$) phase setting was employed. **c-d)** B_1^+ distributions in an axial slice of maximum central B_1^+ . SAR1g distribution ($P_{in} = 1W$) at **e-f)** the surface of the voxel model and **g-h)** through the axial slice of maximum SAR1g. The circle in **g-h)** illustrates the phantom material (Table II) positioned around Duke's head. Please note that the shoulders of Duke were included in the EMF simulations.

Figure 11: Comparison of EMF simulations obtained for the human voxel model Ella including or excluding the bore (inner diameter = 684mm) at 300 MHz and at 1 GHz. EMF simulations were performed for a **a)** 8-element bow tie dipole array at 300 MHz and **b)** the 20-element dipole array at 1 GHz. **c-d)** Absolute E-field distribution (CP) without the bore for 300 MHz and 1 GHz. **e-f)** Absolute E-field distribution (CP) with the bore present at 300 MHz and 1 GHz. Radiation losses increase from 13% (e) at 300 MHz to 29% at 1 GHz (f).

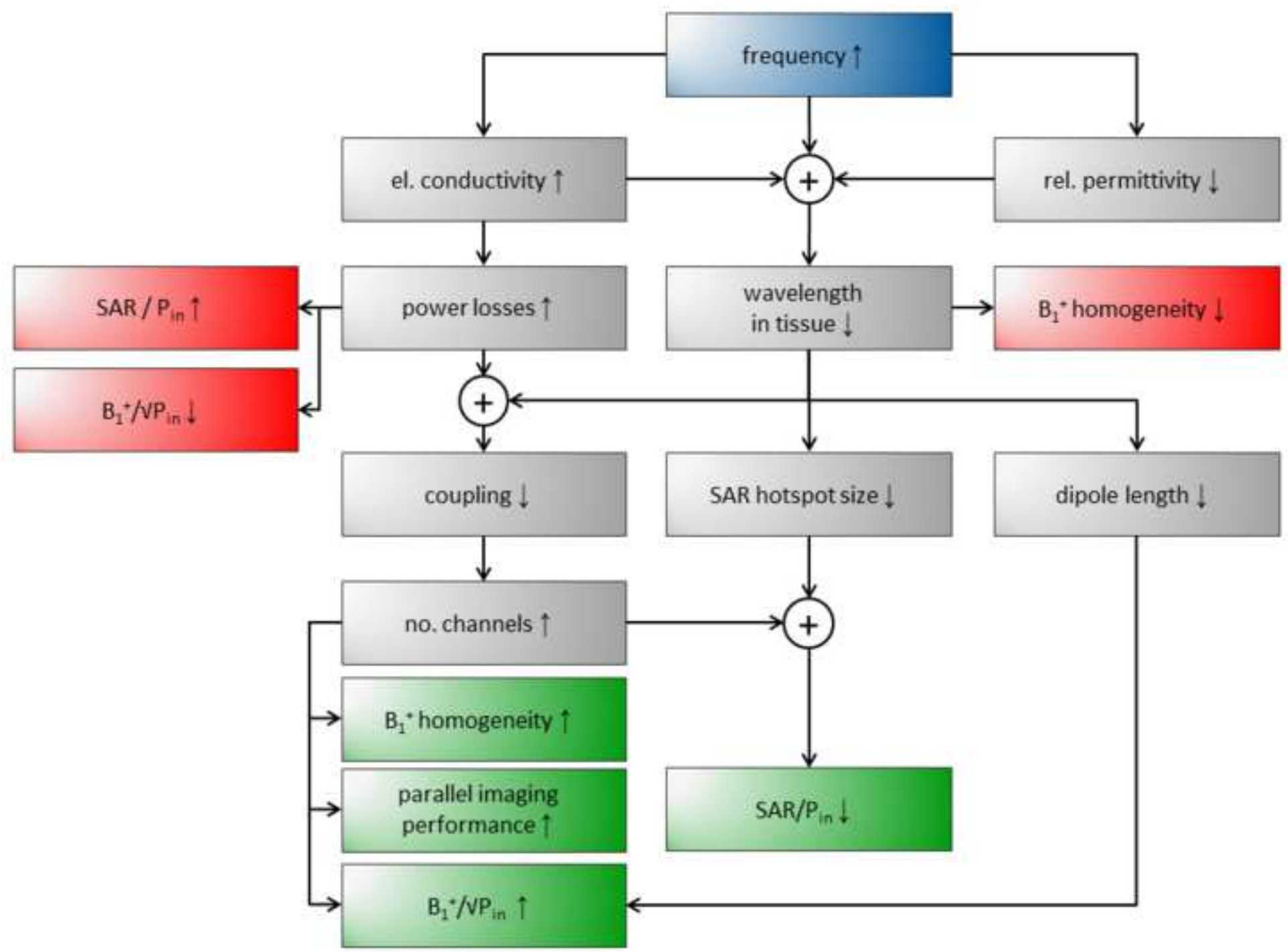
Tables

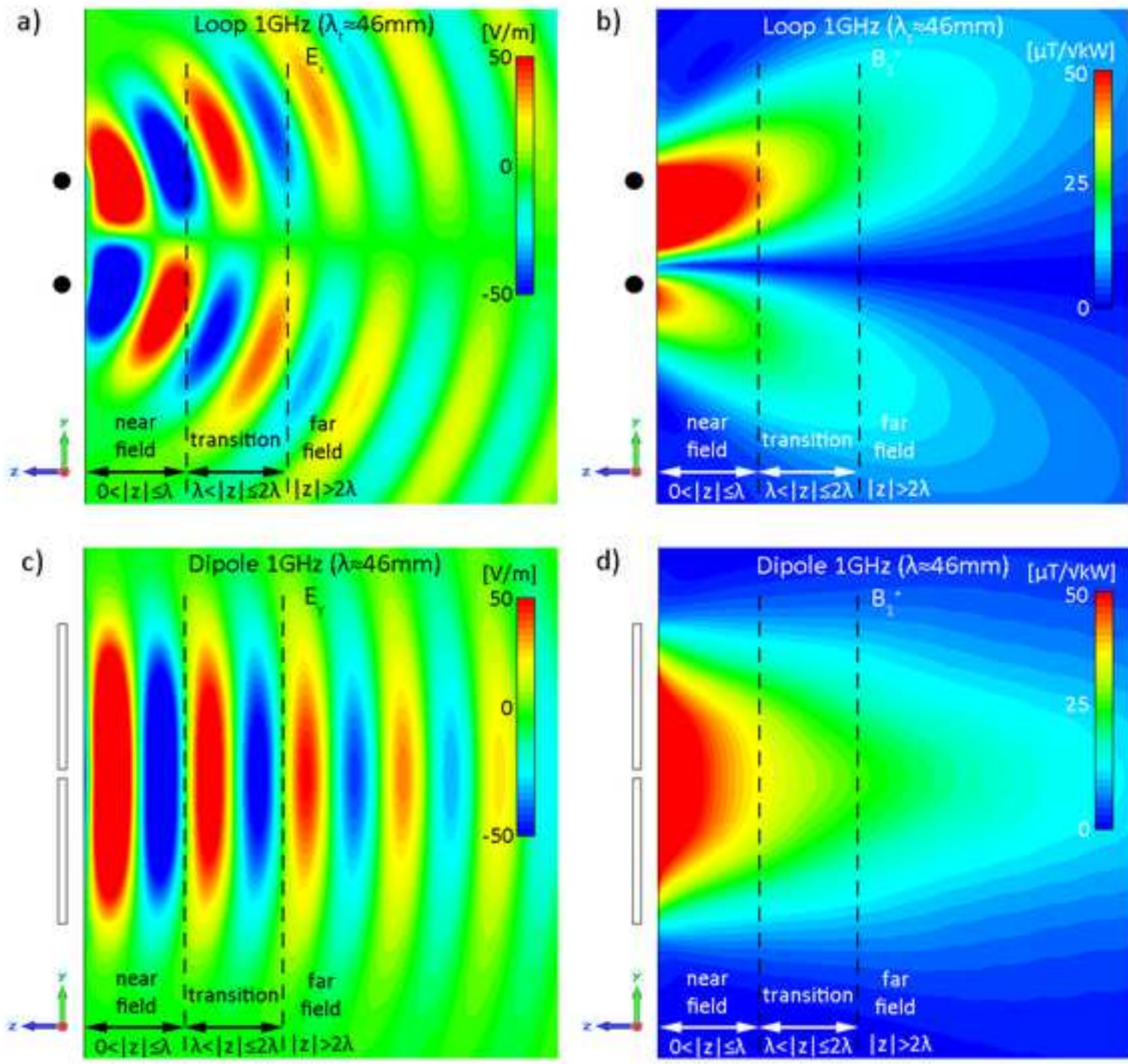
| frequency [MHz] | permittivity | conductivity [S/m] | antenna length [mm] | max channels |
|-----------------|--------------|--------------------|---------------------|--------------|
| 300 | 50.3 | 0.52 | 410 | 8 |
| 400 | 48.2 | 0.57 | 290 | |
| 500 | 46.9 | 0.59 | 260 | |
| 600 | 46.1 | 0.61 | 220 | |
| 700 | 45.4 | 0.66 | 195 | |
| 800 | 44.9 | 0.70 | 172 | |
| 900 | 44.4 | 0.73 | 157 | |
| 1000 | 44.1 | 0.77 | 142 | 19 |
| 1200 | 43.5 | 0.89 | 117 | |
| 1400 | 43 | 0.92 | 102 | |
| 1600 | 42.6 | 1.01 | 87 | |
| 1800 | 42.2 | 1.11 | 77 | |
| 2000 | 41.9 | 1.2 | 69 | 22 |
| 3000 | 40.5 | 1.79 | 44 | 22 |

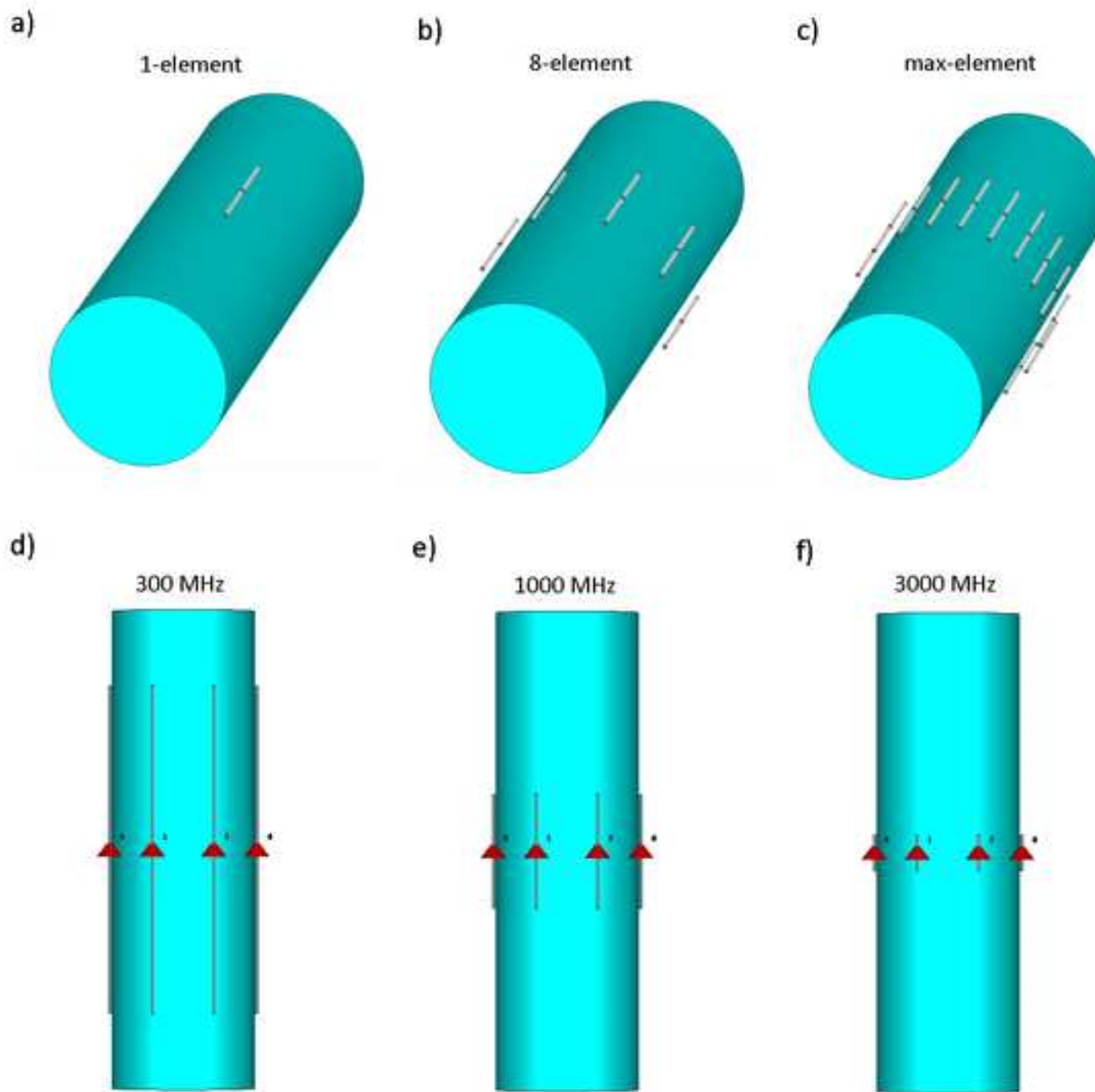
Table I: Electromagnetic properties (permittivity and electrical conductivity) of the phantom used in the simulation study together with the total dipole antenna length. The electromagnetic properties were determined assuming a 60:40 white and grey matter ratio at the given frequencies (66). The inner diameter of all antenna arrays was 196mm.

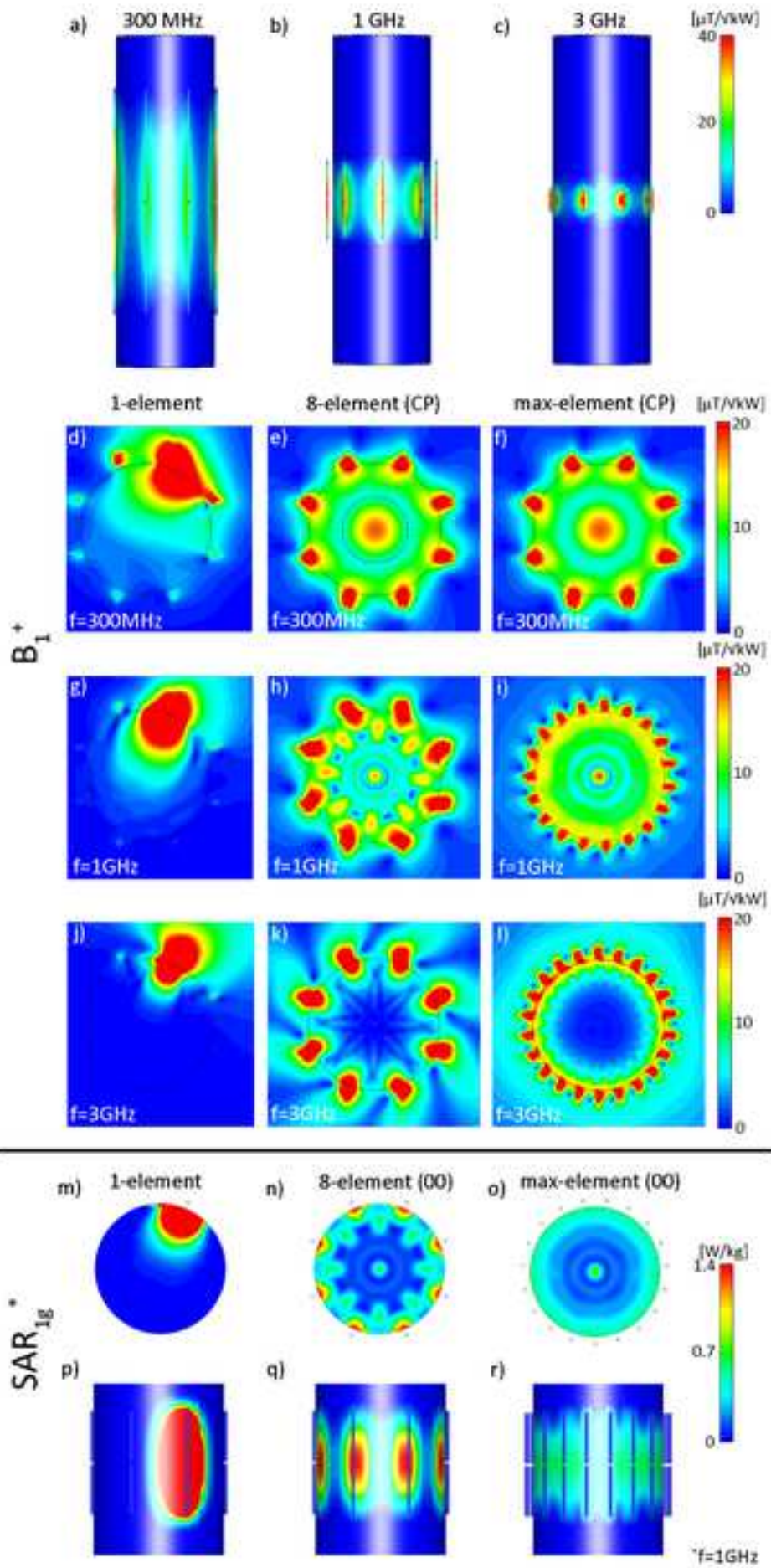
| Tissue | permittivity | | electrical conductivity [S/m] | | density [kg/m ³] |
|---------------------|--------------|------|----------------------------------|------|---------------------------------|
| | 300MHz | 1GHz | 300MHz | 1GHz | |
| white matter | 43.8 | 38.6 | 0.41 | 0.62 | 1041 |
| grey matter | 60 | 52.3 | 0.69 | 0.99 | 1045 |
| blood | 65.7 | 61.1 | 1.32 | 1.58 | 1060 |
| cerebrospinal fluid | 72.7 | 68.4 | 2.22 | 2.46 | 1007 |
| skull | 13.4 | 12.4 | 0.08 | 0.16 | 1908 |
| phantom | 50.3 | 44.1 | 0.1 | 0.1 | - |

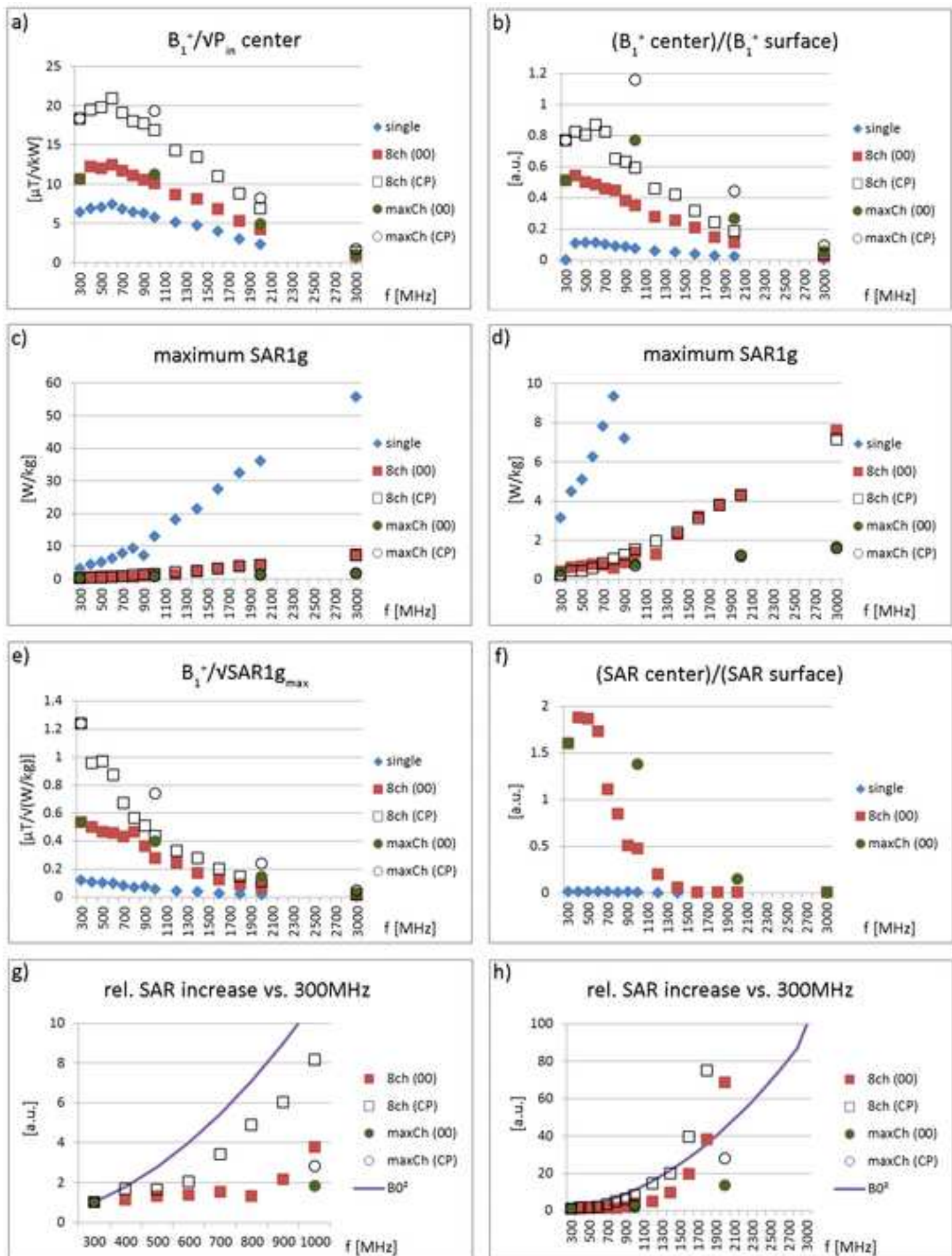
Table II: Representative electromagnetic tissue properties used in the human voxel model simulations. All other parameters used for the voxel model Ella can be found in (66).

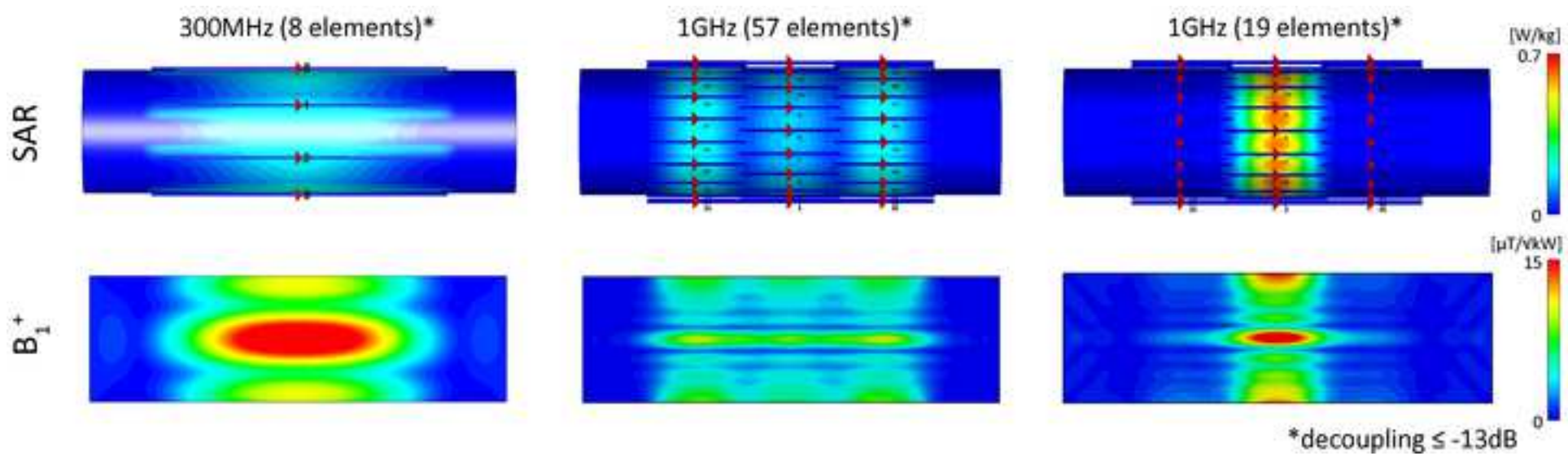




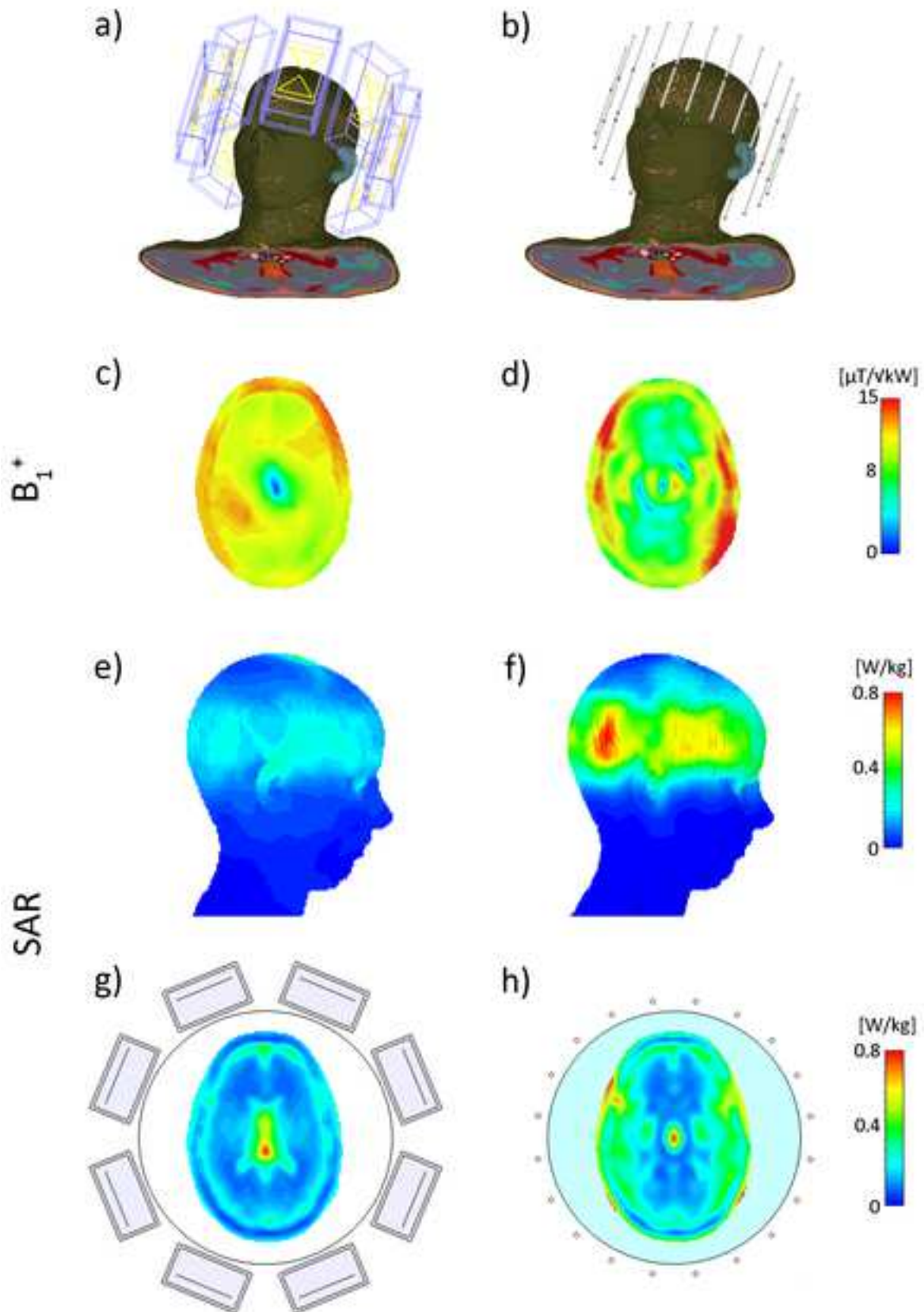


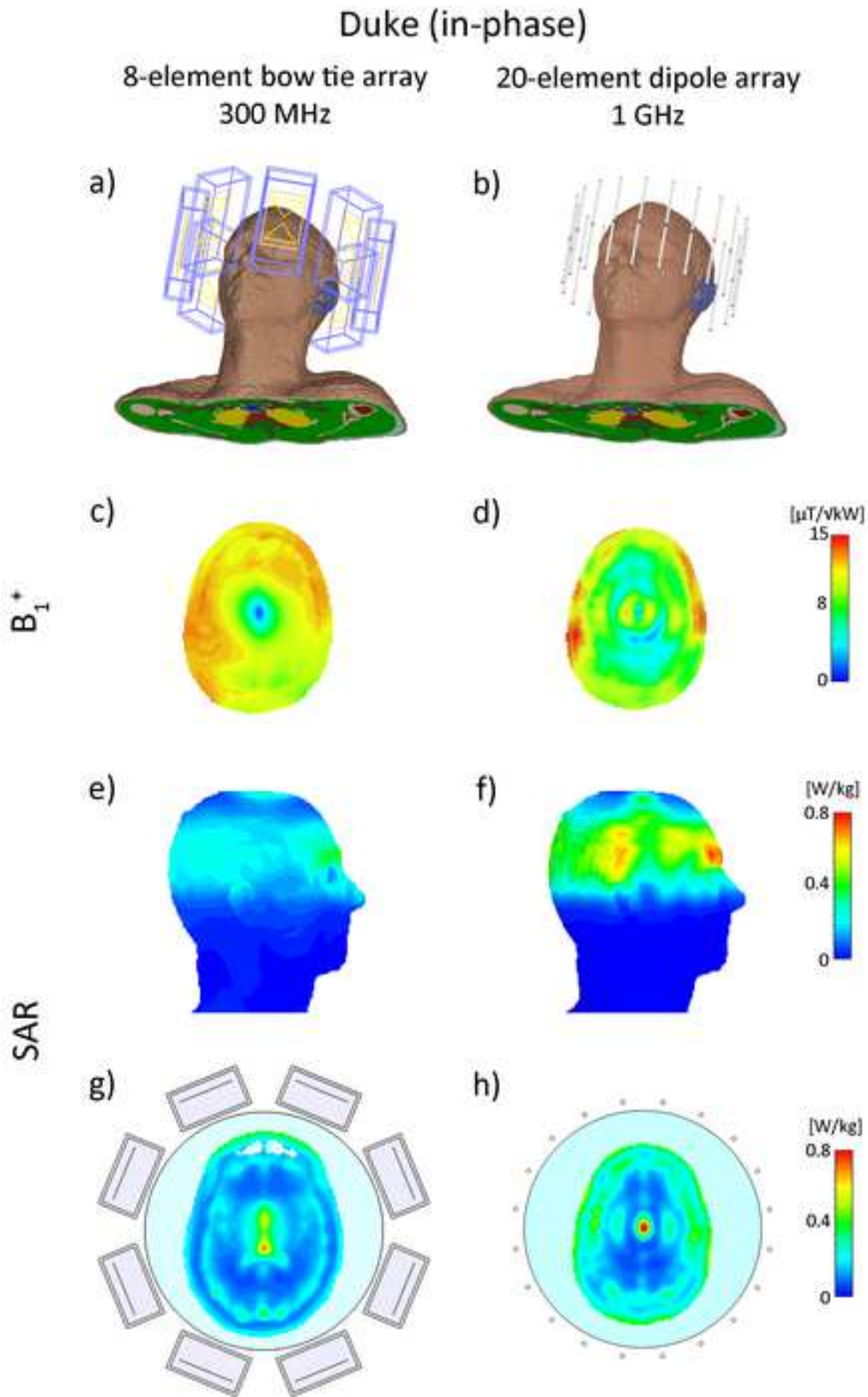




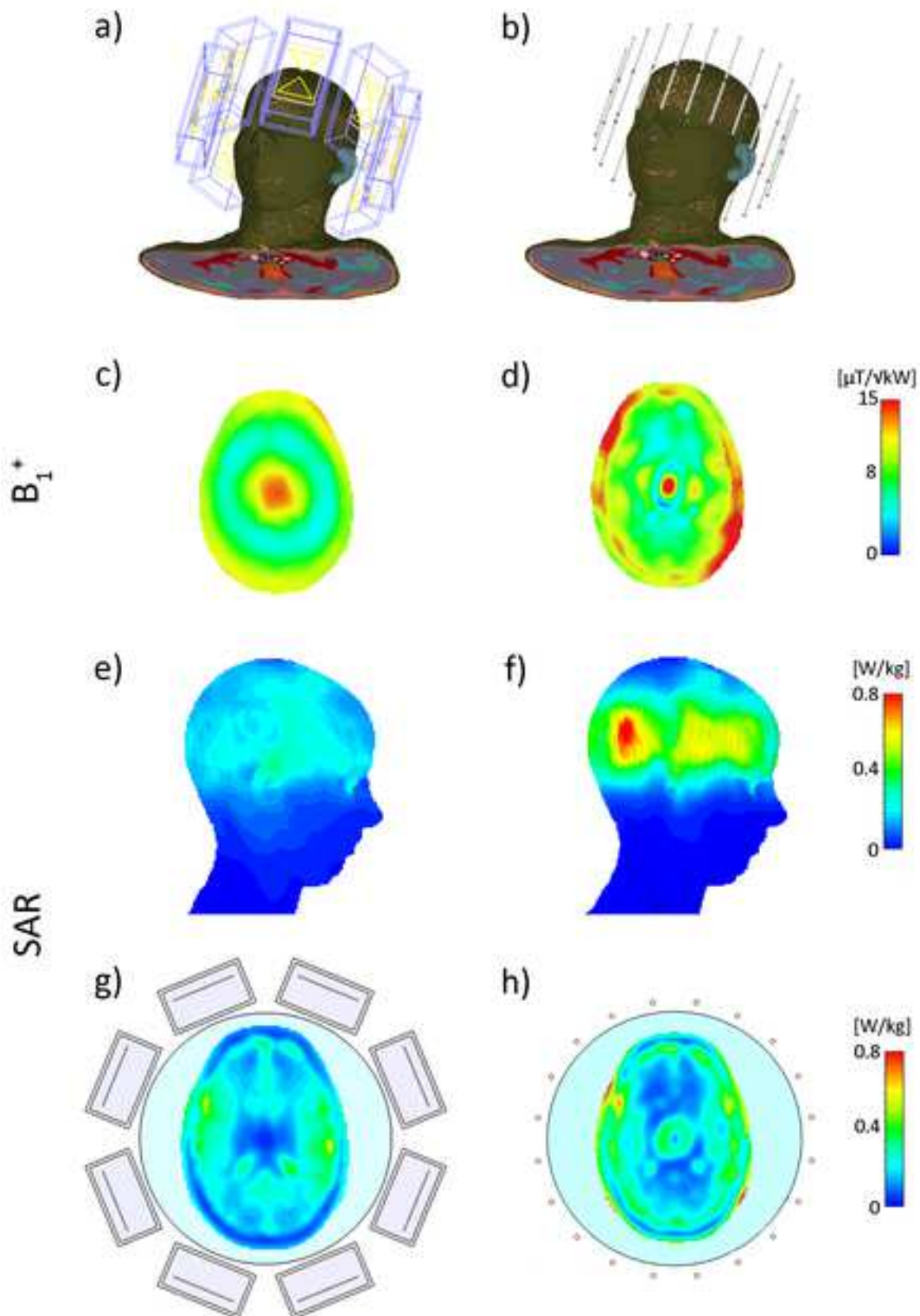


Ella (in-phase)

8-element bow tie array
300 MHz20-element dipole array
1 GHz



Ella (CP)

8-element bow tie array
300 MHz20-element dipole array
1 GHz

Duke (CP)

8-element bow tie array
300 MHz

20-element dipole array
1 GHz

